

Bridge-rich and loop-less hydrogel networks through suppressed micellization of multiblock polyelectrolytes

Received: 25 October 2023

Accepted: 24 July 2024

Published online: 02 August 2024



Jihoon Han^{1,13}, Saeed Najafi^{2,3,13}, Youyoung Byun⁴, Lester Geonzon⁵, Seung-Hwan Oh⁶, Jiwon Park⁴, Jun Mo Koo⁷, Jehan Kim⁸, Taehun Chung¹, Im Kyung Han¹, Suhun Chae⁹, Dong Woo Cho⁹, Jinah Jang⁹, Unyong Jeong¹, Glenn H. Fredrickson^{3,10}, Soo-Hyung Choi⁶, Koichi Mayumi^{5,11}, Eunji Lee⁴✉, Joan-Emma Shea^{2,12}✉ & Youn Soo Kim¹✉

Most triblock copolymer-based physical hydrogels form three-dimensional networks through micellar packing, and formation of polymer loops represents a topological defect that diminishes hydrogel elasticity. This effect can be mitigated by maximizing the fraction of elastically effective bridges in the hydrogel network. Herein, we report hydrogels constructed by complexing oppositely charged multiblock copolymers designed with a sequence pattern that maximizes the entropic and enthalpic penalty of micellization. These copolymers self-assemble into branched and bridge-rich network units (netmers), instead of forming sparsely interlinked micelles. We find that the storage modulus of the netmer-based hydrogel is 11.5 times higher than that of the micelle-based hydrogel. Complementary coarse grained molecular dynamics simulations reveal that in the netmer-based hydrogels, the numbers of charge-complexed nodes and mechanically reinforcing bridges increase substantially relative to micelle-based hydrogels.

Network frameworks in organisms are created through hierarchical self-assembly and defect-free interlinking of biopolymers such as actin, collagen, and mucin^{1–5}. The primary function of a network is to give the organism its shape and mechanical resistance to deformation. In addition, biopolymers self-assemble into intricate network structures that exhibit differentiated functionality. For example, F-actin, a microfilament constituting the intracellular cytoskeleton, is a complex

and dynamic network that supports biological processes such as cell migration and contractile dynamics³. Collagen, the most abundant microfiber in the extracellular matrix, gives a wide range of stiffness and elasticity, from soft skin to hard bone tissues⁴. Mucins assemble into branched networks and form mucus hydrogels, which are responsible for molecular transport and a physical barrier preventing infection⁵.

¹Department of Materials Science and Engineering, Pohang University of Science and Technology (POSTECH), Pohang, Gyeongbuk, Republic of Korea.

²Department of Chemistry and Biochemistry, University of California, Santa Barbara, California, USA. ³Materials Research Laboratory, University of California, Santa Barbara, California, USA. ⁴School of Materials Science and Engineering, Gwangju Institute of Science and Technology (GIST), Gwangju, Republic of Korea. ⁵The Institute for Solid State Physics, The University of Tokyo, Kashiwa, Chiba, Japan. ⁶Department of Chemical Engineering, Hongik University, Seoul, Republic of Korea. ⁷Department of Organic Materials Engineering, Chungnam National University, Daejeon, Republic of Korea. ⁸Pohang Accelerator Laboratory, Pohang University of Science and Technology (POSTECH), Pohang, Gyeongbuk, Republic of Korea. ⁹Department of Mechanical Engineering, Pohang University of Science and Technology (POSTECH), Pohang, Gyeongbuk, Republic of Korea. ¹⁰Department of Chemical Engineering, University of California, Santa Barbara, California, USA. ¹¹Department of Advanced Materials Science, Graduate School of Frontier Sciences, The University of Tokyo, Kashiwa, Chiba, Japan. ¹²Department of Physics, University of California, Santa Barbara, California, USA. ¹³These authors contributed equally: Jihoon Han, Saeed Najafi. ✉e-mail: eunjilee@gist.ac.kr; shea@ucsb.edu; ysookim@postech.ac.kr

Chemical and topological structures of polymers together dictate the properties of networks^{6,7}. Polymer network topology indicates the extent to which the strands of polymers are connected. Given that the elasticity of polymer networks has topological origins, there is a growing interest in understanding and controlling topology from a molecular perspective in order to design networks with specific mechanical properties. Inspired by biological networks, attempts have been made to mimic the network structure in organisms using synthetic polymers^{8–12}. However, these efforts have not been fully successful due to the emergence of topological defects in the network (e.g., inhomogeneity in node/strand density, dangling/unreacted strands and/or entanglements, and loop formation)^{13,14}. Primary loops, the simplest cyclic topologies, form when the two ends of a strand reside in the same node. Since the loops do not impose direct physical crosslinks between nodes, they only weakly contribute to the elasticity of the network through the rare loop entanglement of interlocked polymers from independent nodes¹⁵.

A common approach to designing hydrogel network forming block copolymers is to use an ABA triblock construct wherein the middle and end blocks are hydrophilic and charged blocks, respectively^{16–19}. Mixtures of oppositely charged ABA triblock copolymers assemble through electrostatic interactions and can produce distinct micellar structures in which the coacervate nodes of the

micelles are surrounded by loops formed by the hydrophilic middle blocks. At concentrations higher than the critical gelation concentration (CGC), some loops of the micelles can transform into bridges that connect the coacervate nodes, leading to the formation of a sparsely linked network (Fig. 1a). Therefore, the key components affecting the mechanical properties of ABA triblock hydrogels are the density of bridges and nodes in the network rather than that of loops^{15,20}. Previous observations have shown that the density of bridges increases with increasing relative length of the middle block and concentration of ABA triblock copolymers^{21,22}. However, despite numerous efforts, there appears to be a limit to maximizing the fraction of bridges based on the loop-rich micelle structure, with the largest reported bridge fraction being only 63% in a hydrogel²². In addition, even when the loop formation was suppressed with the ABC triblock terpolymer through independent crosslinking of the A and C blocks, the mechanical properties of the hydrogel were not significantly improved^{23,24}. These observations point to the need for a design strategy for strong hydrogels that focuses less on micellar loops and more on forming bridges. Hence, we aim here to design block polyelectrolytes that directly assemble to form a network of highly interlinked nodes with minimal formation of loops. In this design, it is the bridging process that imparts strong mechanical properties to the resulting network (Fig. 1b). We start with a conventional mixture of triblock

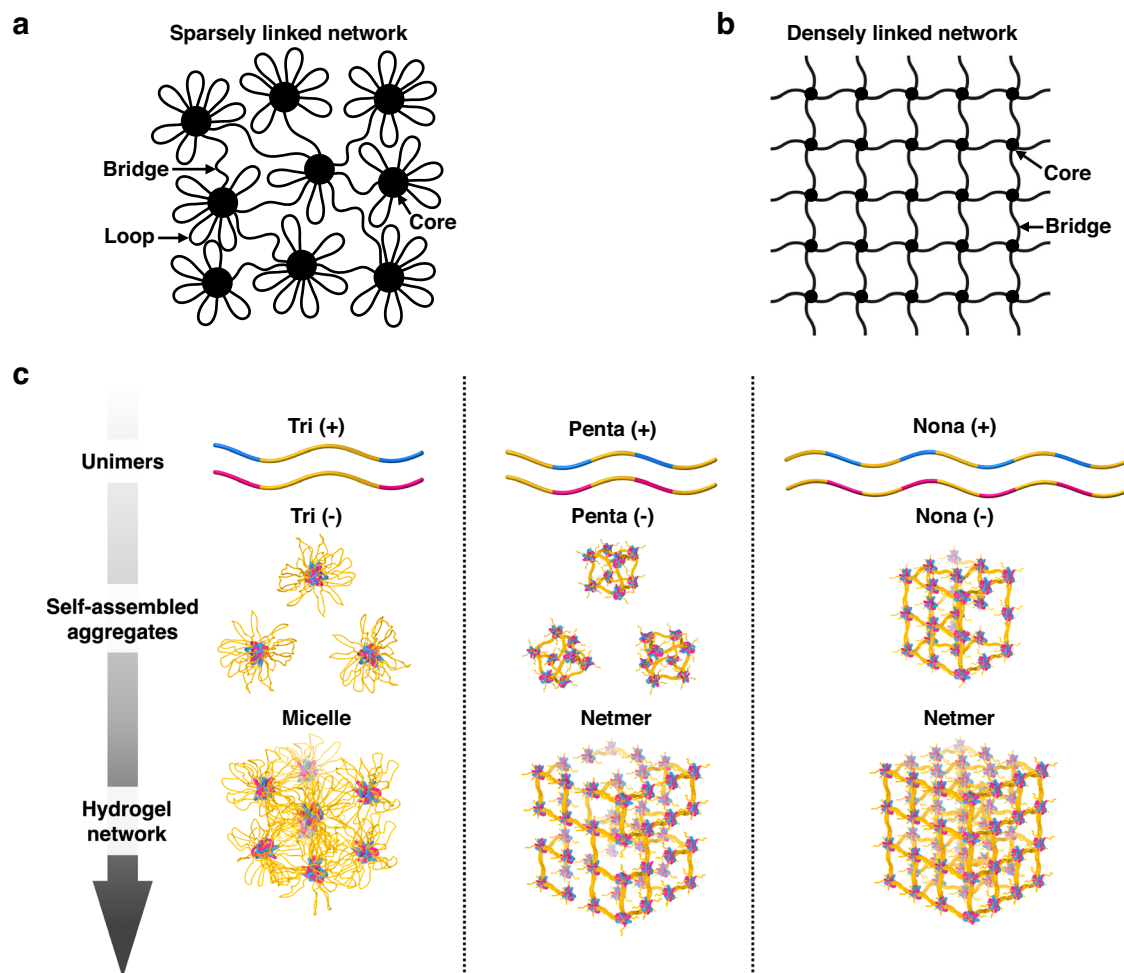


Fig. 1 | Schematic representation of the network structures and gelation mechanisms. Two types of hydrogel networks. **a** In the traditional hydrogel network formed through the self-assembly of ABA block copolymers, the nodes are surrounded by loops. **b** In the proposed densely linked network, the coacervate nodes are closely linked by a large number of bridges. **c** Schematic of the hierarchical assembly mechanism from the unimer to the hydrogel network in three

different polyelectrolytes. As the polymer concentration increased, the triblock polyelectrolytes formed micelles, leading to the formation of a tri-PEC (polyelectrolyte complex) hydrogel network with a sparsely linked structure. Pentablock polyelectrolytes and nonablock polyelectrolytes preferentially formed netmers with branched structures and produced the densely linked penta- and nona-PEC hydrogel networks, respectively.

polyelectrolytes (P(APTC₁₅₀-*b*-DMA₇₅₀-*b*-APTC₁₅₀) and P(AMPS₁₅₀-*b*-DMA₇₅₀-*b*-AMPS₁₅₀)), which will serve as a point of comparison for designed pentablock (P(DMA₂₅₀-*b*-APTC₁₅₀-*b*-DMA₂₅₀-*b*-APTC₁₅₀-*b*-DMA₂₅₀) and P(DMA₂₅₀-*b*-AMPS₁₅₀-*b*-DMA₂₅₀-*b*-AMPS₁₅₀-*b*-DMA₂₅₀)) and nonablock polyelectrolytes (P(DMA₂₅₀-*b*-APTC₁₅₀-*b*-DMA₂₅₀-*b*-APTC₁₅₀-*b*-DMA₂₅₀-*b*-APTC₁₅₀-*b*-DMA₂₅₀-*b*-APTC₁₅₀-*b*-DMA₂₅₀) and P(DMA₂₅₀-*b*-AMPS₁₅₀-*b*-DMA₂₅₀-*b*-AMPS₁₅₀-*b*-DMA₂₅₀-*b*-AMPS₁₅₀-*b*-DMA₂₅₀-*b*-AMPS₁₅₀-*b*-DMA₂₅₀)). Constructs of triblock and pentablock polyelectrolytes with identical molecular weight and charge density per chain were synthesized to compare equivalent polymer counts at the same weight percentage, as shown in Supplementary Fig. 1a, c (note that the length of every neutral block in pentablock polyelectrolytes is one-third of the middle neutral block of triblock polyelectrolytes). We aimed to increase the thermodynamic penalty of micellization in pentablock polyelectrolytes to create another self-assembly²⁵. The design strategy was to increase the bending energy cost of loop formation by introducing short middle neutral blocks and disrupting the associativity of charged termini (that are responsible for loop closure) by replacing them with neutral blocks²⁶. Consequently, the self-assembled pentablock polyelectrolytes exhibit a structural distinction, in which a branched network unit (netmer) with several densely interlinked coacervate nodes was formed instead of barely linked micelles. At concentrations above the CGC, the triblock polyelectrolytes formed a sparsely linked network of micelles (Fig. 1c). Meanwhile, the pentablock polyelectrolytes formed a densely linked network by hierarchically stacking the netmers (Fig. 1c). To further increase gelation efficiency, we designed the longer nonablock polyelectrolytes (composed of the same block species and block molecular weights present in the pentablock polyelectrolytes); the gelation efficiency was maximized due to the formation of larger netmers (Supplementary Fig. 1d, c). The nonablock polyelectrolytes with longer chain lengths can promote the formation of a larger number of linked coacervate nodes per netmer relative to the pentablock polyelectrolytes. Due to the structural advantages of the more highly connected networks of the pentablock and nonablock polyelectrolytes, the storage modulus of the resulting hydrogels was substantially greater than that of the conventional triblock polyelectrolyte hydrogels.

Results and discussion

To achieve a nearly complete monomer conversion, all multi-block polyelectrolytes (Supplementary Fig. 1) were synthesized from acrylamide derivatives with high propagation rate coefficients (k_p) through the one-pot aqueous reversible addition-fragmentation chain transfer (RAFT) polymerization^{27–29}. A well-controlled sequence was successfully obtained for each block with a desired monomer conversion, degree of polymerization, and polydispersity index (PDI), as confirmed by ¹H nuclear magnetic resonance (NMR) and gel permeation chromatography (GPC) (Supplementary Figs. 2–4; details of the synthesis procedure are provided in the Methods section). In this study, four types of multiblock polyelectrolytes were compared as follows (Supplementary Fig. 1). First, triblock and pentablock polyelectrolytes with the same overall length of the polymer were compared (Supplementary Fig. 1a, c). At this time, the length of the middle block of the triblock polyelectrolytes was three times longer than that of the pentablock polyelectrolytes, such that the triblock polyelectrolytes were referred to as tri(long middle, LM)block polyelectrolytes. In addition, we designed triblock polyelectrolytes with the same length as the middle block of the pentablock polyelectrolytes (this is referred to as tri(short middle, SM)block polyelectrolytes, (P(APTC₁₅₀-*b*-DMA₂₅₀-*b*-APTC₁₅₀) and P(AMPS₁₅₀-*b*-DMA₂₅₀-*b*-AMPS₁₅₀))) and determined the effect of the middle block length on the mechanical properties of polyelectrolyte complex hydrogels (Supplementary Fig. 1b). Finally, we designed nonablock polyelectrolytes composed of the same blocks present in the pentablock polyelectrolytes but with increased blocks,

and compared it with other multiblock polyelectrolytes (Supplementary Fig. 1d).

Self-assembled structures at concentrations below the CGC

To determine the tri(LM)block, tri(SM)block, pentablock, and nonablock polyelectrolytes self-assembled complex structures (referred to as tri(LM)-, tri(SM)-, penta-, and nona-PEC (polyelectrolyte complex), respectively), cryo-TEM, SANS, and multiangle DLS experiments were performed for 0.2 wt% PEC solutions. First, 0.2 wt% PECs were visualized by cryo-TEM observations (Fig. 2a–d and Supplementary Fig. 5a–d). All PECs formed spheroid coacervate nodes, penta- and nona-PEC had a small node diameter (23.85 ± 3.66 nm and 21.64 ± 3.75 nm, respectively), but tri(LM)- and tri(SM)-PEC had a large coacervate node diameter (31.14 ± 5.51 nm and 33.84 ± 6.39 nm, respectively) (Fig. 2e–h). Noteworthy, although the ionic blocks of all polyelectrolytes have the same length, the tri(LM)- and tri(SM)-PEC node diameter is larger than that of the penta- and nona-PEC. It is considered that the sequence of each multiblock polyelectrolyte acts as an important factor in forming a node and determining its size. This trend is consistent with theoretical expectations, considering the steric constraints and potential conformations of the ionic blocks within the node structure (Fig. 2l, m)²⁶. In particular, tri(LM)- and tri(SM)-PEC, which feature ionic blocks terminated within the polymer chain, promote the formation of larger nodes by accommodating a conformation with a radius corresponding to the ionic block length. In contrast, penta- and nona-PEC, which have an ionic block sandwiched between two neutral blocks, supposedly result in a more compact node structure due to the steric hindrance imparted by the neutral blocks. The structural analysis of the node of PECs was also confirmed through small-angle neutron scattering (SANS) experiments in 0.2 wt% PEC solutions, with node diameters of 27.4 ± 9.0 nm for tri(LM)-PEC, 31.8 ± 5.4 nm for tri(SM)-PEC, 22.8 ± 5.2 nm for penta-PEC and 18.2 ± 8.4 nm for nona-PEC (Fig. 2i, j). The coacervate node diameter of each PEC calculated by SANS coincided with trends in the cryo-TEM results. After that, we calculated the aggregation number of the polyelectrolytes to form the coacervate node (aggregation number, 270 for tri(LM)-PEC, 421 for tri(SM)-PEC, 155 for penta-PEC, 79 for nona-PEC) (Fig. 2k). Requiring fewer polymers to form a node means that a higher node density can be achieved under the same polymer concentration conditions. Therefore, penta- and nona-PEC are expected to have significantly higher node density than tri(LM)- and tri(SM)-PEC.

To rationalize and visualize the self-assembly of PECs, we performed coarse-grained molecular dynamics (CGMD) simulations of tri(LM)block, tri(SM)block, pentablock and nonablock polyelectrolytes in which the dense phase of the polymers is in coexistence with the dilute phase (Fig. 3a–c, Supplementary Fig. 6a and Supplementary Movies 1–4). This CG model of polyelectrolytes (see coarse-grained molecular dynamics simulation section in Supplementary Information) was developed to qualitatively assess—rather than quantitatively—the behavior of hydrogels. We employed the CG polymer model in implicit solvent to effectively explore the behavior of PECs on a computationally accessible macroscopic scale while preserving essential physical properties such as charge patterns and molecular weight ratio of polyelectrolytes. We carefully selected parameters such as the strength of electrostatic interactions, the dielectric constant, and the effective temperature to reflect the ambient conditions. As is evident from the representative CGMD snapshots (Fig. 3a–c and Supplementary Fig. 6a), tri(LM)block and tri(SM)block polyelectrolytes mainly self-assemble into loop rich micelles. Most of the neutral blocks in tri(LM)-PEC form loops; however, on average 1–2 bridges can form between a pair of coacervate nodes (Fig. 3d, e), which can impose weak connectivity between micelles resulting in low node density (Fig. 3f). In contrast, loop formation is mostly suppressed in penta-PEC for two reasons: (1) the larger bending energy cost of a shorter middle block closure and (2)

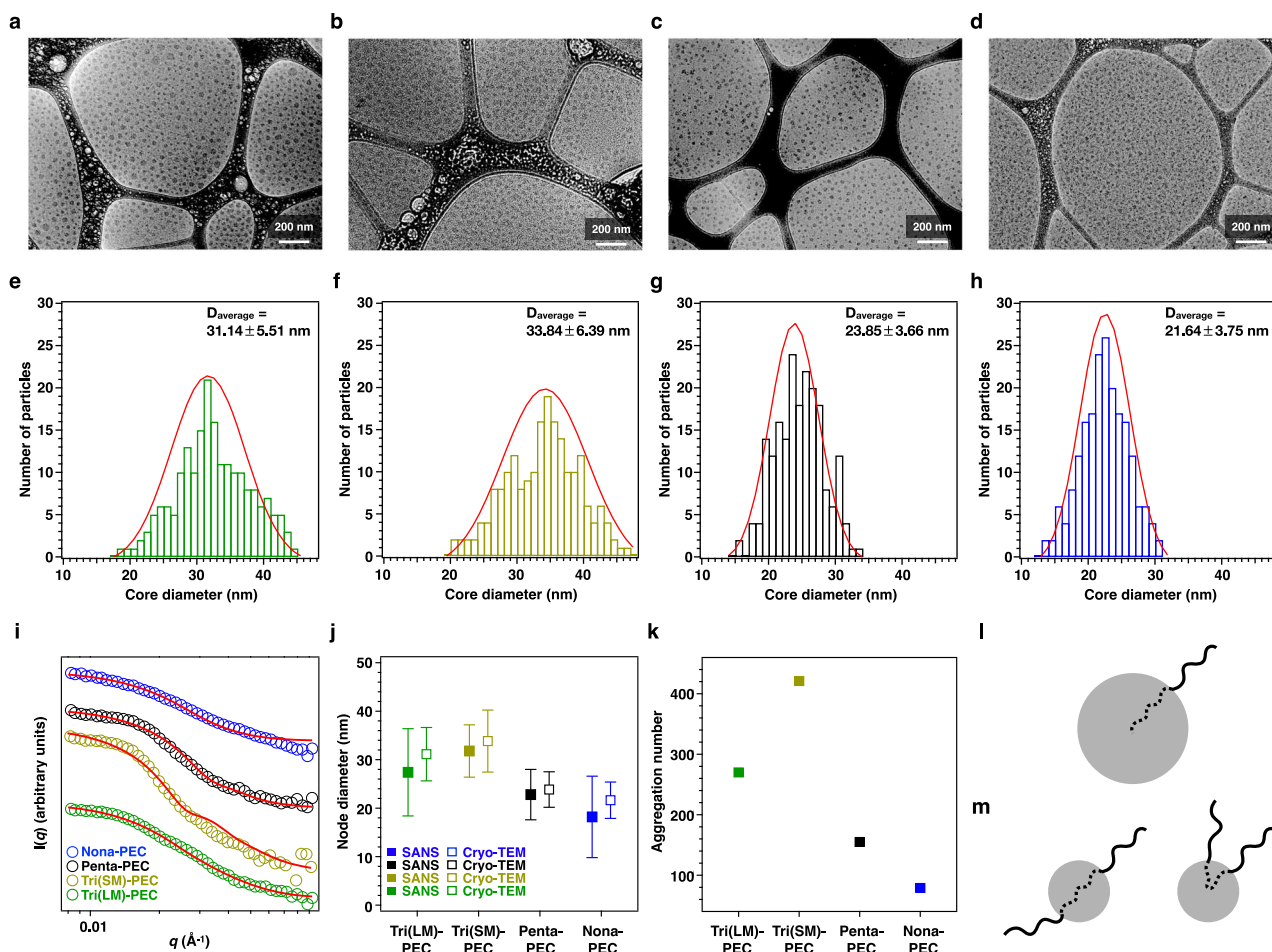


Fig. 2 | Morphology analysis in PEC. Cryo-TEM images of the 0.2 wt% tri(LM)- (a), tri(SM)- (b), penta- (c), and nona-PEC (d). Histogram of core diameter distribution for tri(LM)- (e), tri(SM)- (f), penta- (g), and nona-PEC (h) calculated from cryo-TEM images. The total counts are 200, and the red line is a normal distribution. Core diameters are presented as mean values \pm standard deviation. i SANS profiles of tri(LM)- (green open circles), tri(SM)- (olive green open circles), penta- (black open circles), and nona-PEC (blue open circles) with 0.2 wt% polymer concentration. All SANS profiles were fitted by the best model of the form factor of the core-shell

sphere (red solid line). j Node diameter of four different PECs. The open rectangle represents cryo-TEM results, and the closed rectangle represents SANS results. Node diameters are presented as mean values \pm standard deviation. k Calculated aggregation number of four different PECs. Schematic of the expected ionic block conformations in the coacervate node of tri(LM)- and tri(SM)-PEC (l) and penta- and nona-PEC (m). The gray circle represents the coacervate node, the solid line represents the neutral block, and the dotted line represents the ionic block.

the neutral ends can hamper micellization through hindering interactions with the charged blocks. Thus, in the absence of loop formation, pentablock polyelectrolytes can assemble into netmeric units in which the coacervate nodes are tightly linked through several bridges, resulting in high node density (Fig. 3b and 3d-f). Interestingly, although the length of the neutral block of nonablock polyelectrolytes is as short as that of pentablock and tri(SM)block polyelectrolytes, the larger molecular weight of nonablock polyelectrolytes promotes a richer connection between the coacervate nodes resulting in the highest node density (Fig. 3c-f). In addition to observing differences in the self-assembled form of PECs, we found a significant difference in the node population. In particular, the coacervate nodes of tri(LM)- and tri(SM)-PEC are larger and less numerous than penta- and nona-PEC, see the top right panels of Fig. 3a-c, top left magnified image of Supplementary Fig. 6a (the coacervate nodes are visualized with different colors, for the sake of clarity, the neutral blocks are omitted). Similar to the node size calculated by cryo-TEM and SANS described above, the simulation results also showed that the node size of tri(LM)-PEC was significantly larger than that of penta- and nona-PEC (Supplementary Fig. 7).

Next, a multiangle DLS experiment was conducted to compare the size of the PEC network. The multiangle DLS results revealed mean

decay rate (γ , Γ) was proportional to q^2 in all 0.2 wt% PECs (Fig. 3g and Supplementary Fig. 6b). Therefore, the mutual diffusion coefficient (D_m) of PEC was determined by linear regression of $\Gamma = D_m q^2$ ($D_{\text{tri(LM)-PEC}} = 47,181 \text{ nm}^2/\text{s}$, $D_{\text{penta-PEC}} = 154,460 \text{ nm}^2/\text{s}$, $D_{\text{nona-PEC}} = 85,874 \text{ nm}^2/\text{s}$ and $D_{\text{tri(SM)-PEC}} = 808,810 \text{ nm}^2/\text{s}$). Afterward, the calculated diffusion coefficient was substituted into the Stokes-Einstein equation ($R_h = k_B T / 6\pi\eta_0 D_m$, k_B is the Boltzmann constant, T is the absolute temperature and η_0 is the solvent viscosity, R_h is the hydrodynamic radius) to confirm the hydrodynamic diameter of the PEC network (Fig. 3h and Supplementary Fig. 6c). In the case of tri(LM)-PEC, since the neutral block was made the longest despite a few bridges, connectivity between PEC was secured, creating the largest PEC network ($6.96 \pm 1.38 \mu\text{m}$, Fig. 3h, k). When confirming the tri(LM)-PEC network through CG-MD simulations, a network of sparse and large micelles connected by a few bridges was visible (Supplementary Movie 5). On the other hand, unlike tri(LM)-PEC formed a micelle-based PEC network, penta-PEC formed netmers and its size was $2.13 \pm 0.16 \mu\text{m}$, which was significantly smaller than tri(LM)-PEC (Fig. 3h, i). This means that although penta-PEC is rich in bridges, it has poor connectivity due to short middle blocks and mainly consists of small netmers (Supplementary Movie 6). However, nona-PEC formed larger netmers ($3.82 \pm 0.21 \mu\text{m}$, Fig. 3h, j) than penta-PEC because it had

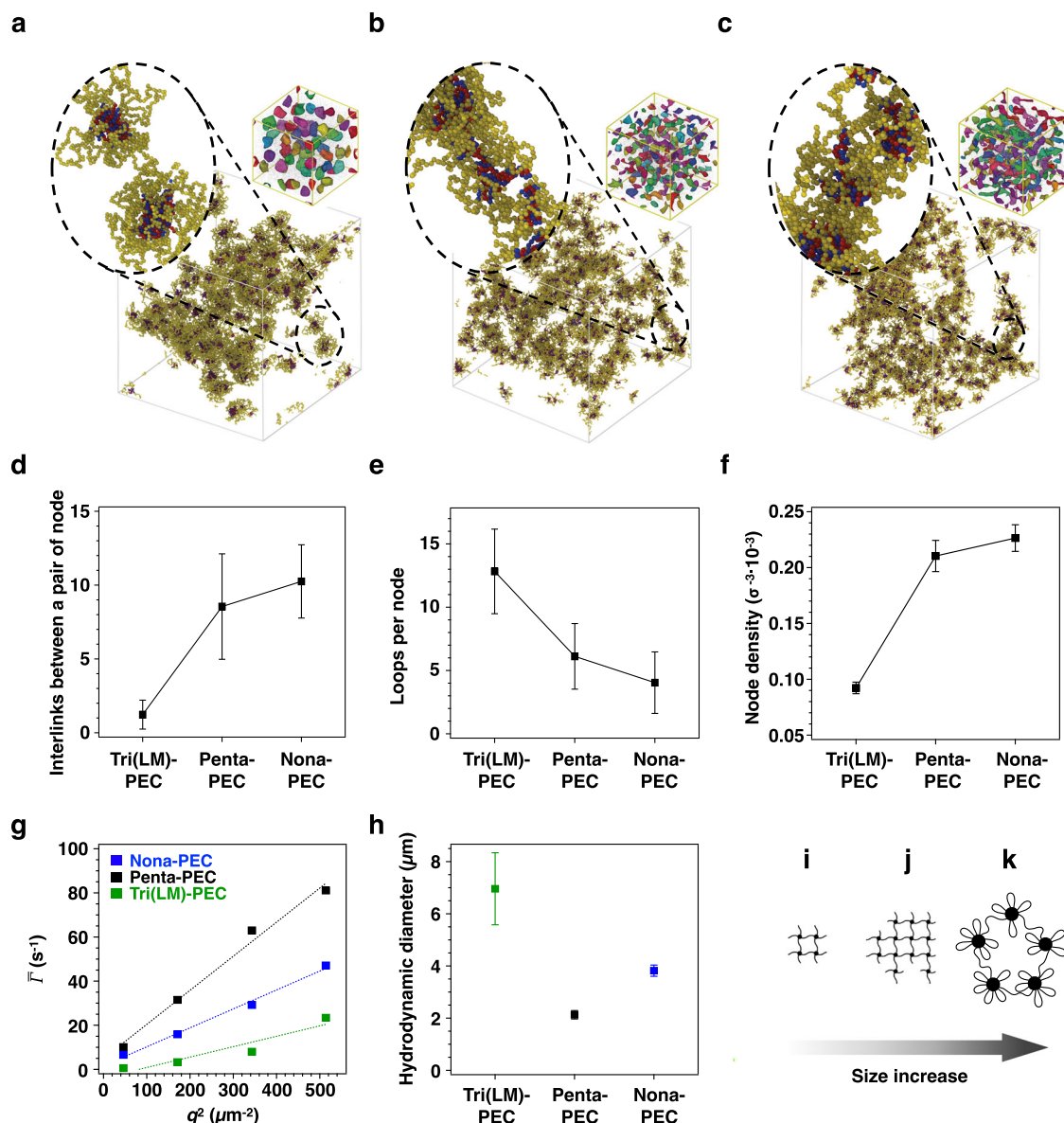


Fig. 3 | CG-MD simulation and size analysis in PEC. Coarse-grained molecular dynamics (CG-MD) simulations of self-assembled tri(LM)- (a), penta- (b), and nona-PEC (c) in coexistence with a dilute phase; the yellow, blue, and red monomers of polymers represent the neutral, negatively charged and positively charged species, respectively. Tri(LM)-PEC showed distinct micellar structures, and penta- and nona-PEC featured largely interlinked coacervate nodes. The coacervate nodes of the PEC in a pure dense phase are shown in the top right of panels, for the sake of clarity, the neutral blocks of the PEC are not shown in the coacervate nodes

visualization. **d** The interlinks between a pair of nodes in three PECs. **e** The number of loops per node in three PECs. **f** The node density of three PECs in the dense phase. **g** Corresponding q^2 dependence of the mean decay rate (γ , Γ) for three PECs from multiangle DLS experiments. **h** Comparison of hydrodynamic diameter for three PECs. Schematic of the expected PEC cluster structure for penta- (i), nona- (j), and tri(LM)-PEC (k). CG-MD simulation data and hydrodynamic diameter are presented as mean values \pm standard deviation.

four ionic blocks within one polymer to ensure connectivity. Accordingly, the nona-PEC network showed a tight, densely connected network conformation in CG-MD simulations (Supplementary Movie 7). Meanwhile, in the case of tri(SM)-PEC, the smallest PEC network was shown due to the small number of bridges and short middle block ($0.40 \pm 0.05 \mu m$, Supplementary Fig. 6c, d). These results show differences in PEC network morphology depending on the polymer structure, which may affect gelation efficiency and mechanical properties at high polymer concentrations^{6,7}.

PEC hydrogels at concentrations above the CGC

After analyzing the diluted solutions of tri(LM)-, tri(SM)-, penta-, and nona-PEC, we systematically investigated the mechanical

properties of the PEC hydrogels. First, the CGC was confirmed by measuring the change in the zero-shear viscosity according to the concentration (Supplementary Fig. 8)³⁰. In general, the higher the connection efficiency of the network, the lower the CGC. As expected, nona-PEC (0.8 wt%) showed the lowest CGC than other type of PEC. Interestingly, tri(LM)-PEC (1.0 wt%) showed lower CGC than penta-PEC (1.5 wt%). Penta-PEC requires a relatively higher polymer concentration to construct the network networkers; note that tri(LM)-PEC can benefit from the longer middle block to create interlinks at low polymer concentrations. In the case of tri(SM)-PEC, which had a small number of bridges with a short middle block, it showed the highest CGC (3.0 wt%) due to shortcomings in network connectivity.

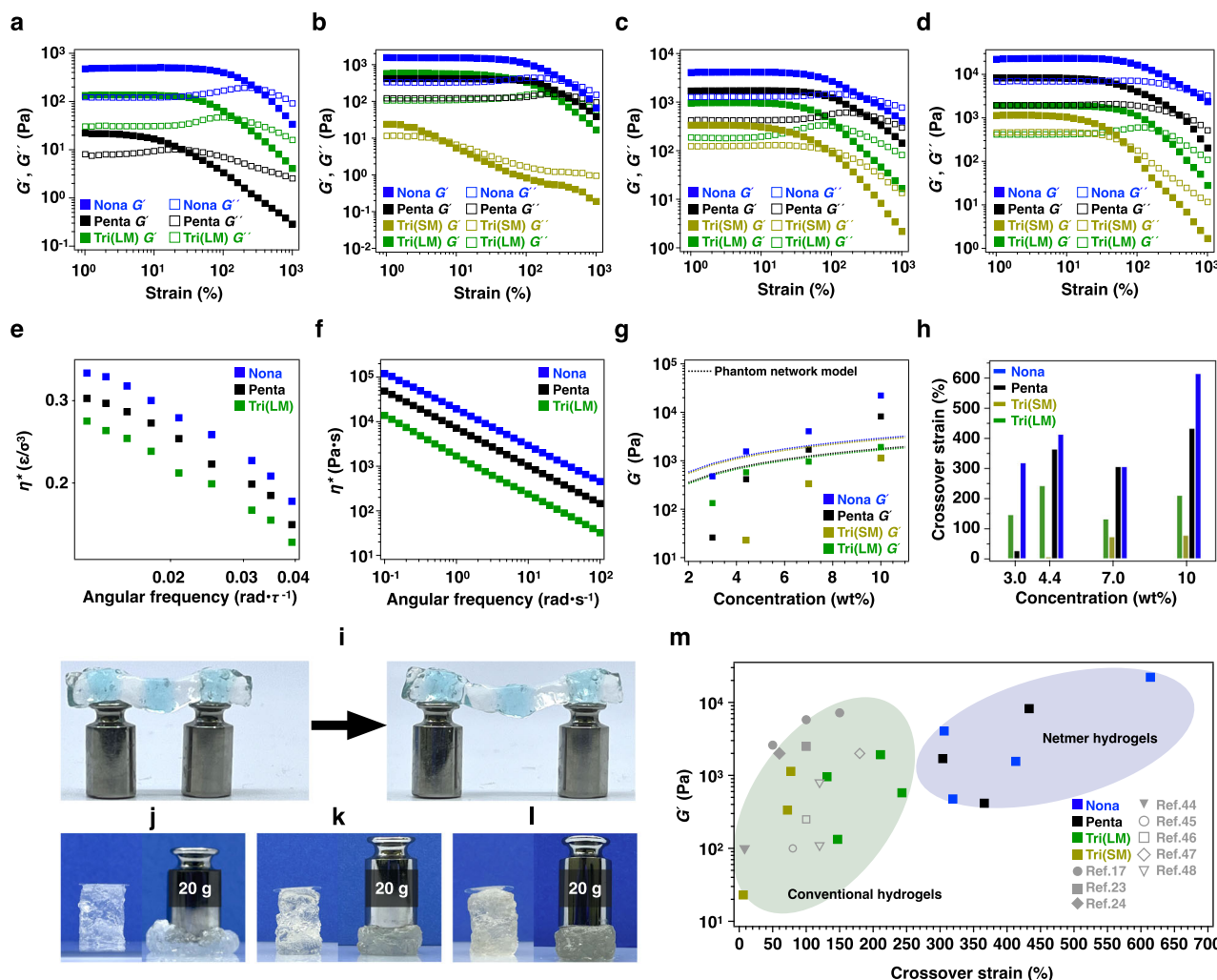


Fig. 4 | Rheological properties of the PEC hydrogels. Strain sweep was performed in a strain range from 1 to 1000% at a frequency of 3 rad s^{-1} . Storage (G' , closed rectangles) and loss (G'' , open rectangles) moduli of the tri(LM)- (green), tri(SM)- (olive green), penta- (black), and nona-PEC (blue) hydrogels with 3.0 (a), 4.4 (b), 7.0 (c) and 10.0 wt% (d) polymer concentrations. Angular frequency dependencies of the complex viscosity of the hydrogels from the non-equilibrium CGMD simulations (e) and experiments (f). Rheological properties of the tri(LM)-, tri(SM)-, penta-, and nona-PEC hydrogels with various polymer concentrations. G' obtained at a 1% strain and frequency of 3 rad s^{-1} and the dotted line represents

ideal G' calculated through the phantom network theory of rubber elasticity (g) and crossover strains of the G' and G'' determined from the strain amplitude sweep measurement (h). i Free-standing and stretchable performance of nona-PEC hydrogels with and without blue dye in the form of cubes. 20 g weighted cube-shaped 10.0 wt% tri(LM)- (j), penta- (k) and nona-PEC (l) hydrogels. m PEC hydrogels compared to synthetic and natural hydrogels. Gray closed labels represent synthetic block copolymer hydrogels, and gray open labels represent natural hydrogels, including chitosan, gelatin, lignin, and peptide.

Next, rheological examinations were conducted to determine the viscoelastic properties of the studied hydrogels such as storage modulus (G') and loss modulus (G''), which represent the ability to store energy elastically and dissipate energy through heat, respectively. To investigate the effect of polymer concentration on the mechanical properties of the PEC hydrogels, strain and frequency sweep experiments were conducted for all four types of hydrogels at polymer concentrations ranging from 3.0 to 10.0 wt% (Fig. 4a–d, g, h and Supplementary Figs. 9, 10 (Note that the tri(SM)-PEC experiments were conducted starting from a concentration of 4.4 wt%, measured stably)).

The results revealed that G' was substantially larger than G'' at low strain values, and their intersection was observed at higher strains due to the yielding of the gel. Furthermore, $\tan \delta$ (defined as G''/G' in the linear elastic regime) produced similar values between 0.15 and 0.48 at all polymer concentrations, which indicates that all PEC hydrogels behave more like elastic materials rather than viscous liquids (Supplementary Fig. 9). The G' values and crossover strains

according to the polymer concentration of all hydrogels are summarized in Table 1, Fig. 4g, h. For tri(SM)-PEC hydrogels, as can be expected from previous results, it showed the lowest mechanical properties at all polymer concentrations. Interestingly, G' of tri(LM)-PEC hydrogels was higher than that of penta-PEC hydrogels in the concentration range from 3.0 to 4.4 wt% (Fig. 4a, b), but the trend was reversed from 7.0 wt% (Fig. 4c, d). Thus, at low polymer concentrations, the penta-PEC netmers are less likely to form a hydrogel network; as shown in the CGC of penta-PEC was higher than tri(LM)-PEC. This suggests that at low polymer concentrations, where the gelation force is insufficient for penta-PEC hydrogel formation, longer nona-block polyelectrolytes can utilize their greater molecular weight to enhance spatial correlation among the nodes. This characteristic facilitates gelation through the formation of large netmers, where multiple coacervate nodes are interconnected. These nodes are linked by electrostatic interactions and bridged by neutral blocks, enabling the formation of several coacervate nodes per nonablock polyelectrolyte. Thus, the mechanical properties of nona-PEC hydrogel were

Table 1 | Summary of the mechanical properties of the hydrogels

Hydrogel	Weight Concentration (wt%)	Molar Concentration (μM)	G' at a strain of 1% ^a (Pa)	Crossover strain (%) ^a
Tri(LM)-PEC hydrogel	3	214	133	147
	4.4	314	578	243
	7	499	959	131
	10	714	1924	211
Tri(SM)-PEC hydrogel	4.4	486	23	6
	7	774	335	72
	10	1105	1138	77
Penta-PEC hydrogel	3	214	26	30
	4.4	314	416	366
	7	499	1699	304
	10	714	221	433
Nona-PEC hydrogel	3	118	476	319
	4.4	173	1557	413
	7	275	4065	306
	10	392	22,173	614

^a Determined by strain amplitude sweep at a fixed frequency of 3 rad s⁻¹.

pronounced at low polymer concentrations. For example, at 3.0 wt%, the G' of the nona-PEC hydrogel (476 Pa, 118 μM) was 3.6 times higher than that of the tri(LM)-PEC hydrogel (133 Pa, 214 μM) (Table 1).

At high polymer concentrations, all the netmer clusters were well-connected, and thus, netmer bridges acted as elastic springs^{15,20}. Indeed, at concentrations above 7.0 wt%, G' of penta-PEC hydrogel was larger than G' of tri(LM)-PEC hydrogel (Fig. 4c, d). In particular, at 10.0 wt%, the penta-PEC hydrogel showed G' that was about 4 times greater than that of the tri(LM)-PEC hydrogel. As seen in previous results, penta-PEC had structural advantages over tri(LM)-PEC, such as abundant bridges and high coacervate node density, which benefited the mechanical properties according to rubber elasticity theory^{6,7}. However, these structural advantages were expressed in mechanical properties only if network connectivity was guaranteed¹⁵. Therefore, the structural advantages of the penta-PEC hydrogel began to emerge in the high polymer concentrations (in this case, from 7.0 wt%), where the polymer concentration complemented network connectivity. Note that nona-PEC hydrogel had guaranteed network connectivity and structural advantages even at low polymer concentrations so that at 10.0 wt%, the G' of the nona-PEC hydrogel (22,173 Pa, 392 μM) was 11.5 times higher than that of the tri(LM)-PEC hydrogel (1924 Pa, 714 μM) (Table 1).

Next, the experimentally determined modulus of the hydrogel was compared with the predicted modulus for the 100% bridging network model. For this purpose, based on the phantom network theory of rubber elasticity, assuming that all polymers constituting the hydrogel exist as bridges, G' of the hydrogel was calculated (see Fig. 4g and phantom network theory of rubber elasticity section in Supplementary Information). The experimental G' of tri(LM)- and tri(SM)-PEC hydrogels was similar to or lower than the theoretical G' at all polymer concentrations, which was considered to be a negative deviation caused by the loops present in the actual hydrogel. Interestingly, starting from 7.0 wt% polymer concentration, the penta-PEC hydrogel exhibited an experimental G' much higher than the theoretical G' . It can be expected that the abundance of entanglement between bridges existing between nodes caused positive deviation^{31–33}. In particular, the nona-PEC hydrogel shows an experimental G' greater than the theoretical G' starting at 4.4 wt%, and the difference from the theoretical value becomes larger as the concentration increases. This is because the longest nonablock polyelectrolytes may have more dominant

entanglement between adjacent bridges during the self-assembly process. To computationally assess the mechanical properties of the hydrogels, we performed non-equilibrium (NE) CGMD simulations of polyelectrolytes dense phase under an oscillatory shear deformation (see the Supplementary Fig. 11 and NE-CGMD simulations section in Supplementary Information) and characterized the angular frequency dependency of the complex viscosity (Fig. 4e). The complex viscosities of the hydrogels from NE-CGMD simulations can predict the trend of the experimentally characterized complex viscosities (Fig. 4f).

To gain further insight into the structure of the PEC network, the SAXS profile of the hydrogel was investigated (Supplementary Fig. 12a–d). From the SAXS results, as the polymer concentration was increased from 3.0 to 10.0 wt%, the domain spacing of the three hydrogels decreased; the domain spacing was calculated from the primary scattering peak (defined as $d = 2\pi/q$) (Supplementary Fig. 12e). Over the entire concentration range, the penta-PEC hydrogels possessed a much shorter domain spacing, than that of the tri(LM)-PEC hydrogels due to the shorter neutral blocks between the ionic blocks (Supplementary Fig. 1a, c). Since the tri(SM)block polyelectrolytes had the same neutral block length as the pentablock polyelectrolytes, it showed a domain spacing that was smaller than that of the tri(LM)-PEC hydrogel and similar to that of the penta-PEC hydrogel (Supplementary Fig. 1b). In the case of tri(SM)-PEC hydrogel, domain spacing increased at 10.0 wt% polymer concentration, which means that as the polymer concentration increased, the network structure changed due to the rearrangement of the polymer chains¹⁷. Since tri(SM)-PEC hydrogel had a low molecular weight, the molar concentration at 10.0 wt% was higher than that of other PEC hydrogels, which seemed to accelerate the rearrangement of the polymer chains. Since nonablock polyelectrolytes had high polydispersity, the diversity of chain lengths and sizes caused the scattering vector of nona-PEC hydrogels to spread, resulting in broader peaks in the SAXS profile. Interestingly, at high polymer concentrations, nona-PEC hydrogel displays similar domain spacing to penta-PEC hydrogel due to the same length of neutral blocks (Supplementary Fig. 1c, d). Afterward, diffraction peaks were confirmed at a polymer concentration of 10.0 wt% for all hydrogels (diffraction peaks, q_1 , $\sqrt{3}q_1$ and $\sqrt{12}q_1$ for tri(LM)-PEC hydrogel, q_1 and $\sqrt{7}q_1$ for penta-PEC hydrogel, q_1 for nona-PEC hydrogel and q_1 , $\sqrt{4}q_1$ and $\sqrt{12}q_1$ for tri(SM)-PEC hydrogel). All PEC hydrogels were sufficiently dilute that they only exhibited a disordered structure, rather than ordered mesophases. Future research at higher polymer concentrations will likely be necessary to confirm the ordered structure.

To further explore the network structure dependency of the PEC hydrogel on polymer concentration, two-dimensional correlation spectroscopy (2DCOS) was used by one-dimensional (1D) Raman spectra. By comparing the synchronous and asynchronous 2DCOS spectra, it was possible to confirm the sequential order of various chemical constituents and the transformation of the network structure according to the polymer concentration^{34–37}. In the synchronous 2D Raman correlation spectrum, red peaks mean two correlated peaks change in the same direction (increase or decrease together depending on increasing concentration), whereas blue peaks mean two correlated peaks change in the opposite direction. According to Noda's rule³⁵, in the asynchronous 2D Raman correlation spectrum, if two correlated peaks have the same color at the same position as the synchronous spectrum, the peak on the x-axis changes before the peak on the y-axis according to the change in concentration. If the colors are different, the peak on the y-axis changes before the peak on the x-axis according to the change in concentration. Generally, in the 2DCOS analysis, bonds with a fast sequence are either a bond constituting the main chain of a polymer that undergoes a significant conformational change^{34,38,39} or non-covalent interactions (electrostatic interactions or hydrogen bond) that significantly increase or decrease^{40–43}. The representative Raman bands of our PEC hydrogels were observed at wavenumbers of 2940 (C–H), 1160 (C–N⁺), 1050 (SO₃⁻), 930 cm⁻¹ (C–C)

(Supplementary Figs. 13–16). Upon comparison of the 2DCOS results of the tri(LM)-PEC hydrogels, it was found that the sequential order of the bands upon increasing the polymer concentration was as follows: $C-N^+ < SO_3^- < C-H < C-C$ (Supplementary Fig. 13 and Supplementary Table 13). Furthermore, for tri(SM)-PEC hydrogels, the sequential order of the bands upon increasing the polymer concentration was as follows: $C-N^+ < SO_3^- < C-C < C-H$ (Supplementary Fig. 14 and Supplementary Table 13). In other words, the hydrocarbon bonds that make up the main chain changed more rapidly than those composing the charged blocks, indicating considerable structural changes in the polymer chain. This result is consistent with the conformational change of the polymer chain in the tri(LM)- and tri(SM)-PEC hydrogels, where the micellar loops are transformed into expanded bridges as the polymer concentration increases (Fig. 1c)²². On the other hand, for penta- and nona-PEC hydrogels, the sequential order of the bands upon increasing the polymer concentration was as follows: $C-H < C-C < SO_3^- < C-N^+$ (Supplementary Figs. 15, 16 and Supplementary Table 13). In other words, the bonds that make up the charged blocks changed faster than those in the main chain. Therefore, as the polymer concentration increased, coacervation of the charged blocks occurred predominantly, connecting the netmers hierarchically (Fig. 1c).

Finally, as a simple functional test, we investigated the self-healing properties of the physical hydrogels. As shown in Supplementary Fig. 17a–d, after the strain-induced failure, all hydrogels immediately and completely restored both their G' and G'' , indicating the rapid recovery of the entire network. In particular, the self-healing hydrogels by attaching different nona-PEC hydrogels with and without blue dye in the form of cubes were free-standing and showed good stretchable performance (25% strain) (Fig. 4i). Other PEC hydrogels were also capable of self-healing, but due to their low mechanical properties, they broke easily upon deformation, unlike the nona-PEC hydrogel. In addition, when a weight of 20 g was placed on tri(LM)-, penta-, and nona-PEC cube-shaped 10.0 wt% hydrogels (having similar sizes and heights), there were distinct mechanical responses; tri(LM)-PEC hydrogel (Fig. 4j) failed to withstand the weight and shattered, whereas penta- and nona-PEC hydrogels sustained the stress without failure (Fig. 4k, l). Afterward, we compared the G' and crossover strain of our hydrogels with those of other synthetic and natural hydrogels with physical bonds (Fig. 4m)^{17,23,24,44–48}. Our hydrogel exhibited higher G' and crossover strain than other hydrogels, suggesting that a simple method of controlling the sequence of the multiblock copolymer can improve the quality of the physical hydrogel by maximizing the fraction of elastically effective bridges in the network. We anticipate that our methodology holds significant promise for creating multiblock copolymer-based physical hydrogels with reduced structural defects.

Herein, we demonstrated a simple strategy to produce rigid, water-rich hydrogels through the self-assembly of oppositely charged multiblock polyelectrolytes. Loop formation was inevitable when conventional ABA triblock polyelectrolytes self-assembled into core coacervate micelles, creating topological defects in subsequent network formation. Our strategy was to synthesize pentablock and nonablock polyelectrolytes by adjusting the sequence of linear polymers. As revealed by the CGMD simulations, the pentablock and nonablock polyelectrolytes inhibited loop formation; thereby, these polymers were directly self-assembled into highly branched netmers with several bridges formed between the coacervate nodes. As a result, the mechanical properties of the netmer-based hydrogels were greater than those of the conventional micelle-based hydrogels. Our CGMD simulations and experimental investigation show that linear polymers with appropriate charge sequence modulation can form highly interlinked and mechanically robust networks. Given that, in addition to electrostatic interactions, various physical interactions such as hydrophobic interactions, hydrogen bonding, and metal-ligand coordination can be incorporated into netmer

compositions, we expect further development of robust and physical hydrogels in the future.

Methods

Synthesis of multiblock copolymers by RAFT polymerization

Synthesis of poly(*N,N*-dimethylacrylamide (DMA)). Phosphate buffer solution (6 mL, 10 mM, pH = 7), 4-(((2-carboxyethyl)thio)carbo-
nothiyl)thio-4-cyanopentanoic acid (CETCPA) (17.9 mg, 7.63 mM), DMA (1375 mg, 1.81 M), and 2,2'-azobis(2-methylpropionamide) dihydrochloride (V-50) (1.0 mg, 0.48 mM) were introduced into a 100-mL flask equipped with a magnetic stirrer bar and sealed with a rubber septum to synthesize poly(DMA). The mixture was deoxygenated by freeze–pump–thaw cycling more than three times, after which polymerization was performed at 70°C using a temperature-controlled heating mantle followed by stirring at 60 rpm for 2 h to reach a nearly full conversion. A sample was extracted from the polymerization medium using a degassed syringe for ¹H NMR and GPC analyses to determine the monomer conversion, $M_{n,GPC}$, and \bar{D} values.

Synthesis of poly((3-acrylamidopropyl)trimethyl ammonium chloride (APTC)). Phosphate buffer solution (6 mL, 10 mM, pH = 7), CETCPA (17.9 mg, 6.57 mM), APTC (1805 mg, 0.98 M), and V-50 (3.5 mg, 1.46 mM) were introduced into a 100-mL flask equipped with a magnetic stirrer bar and sealed with a rubber septum to synthesize poly(APTC). The mixture was deoxygenated by freeze–pump–thaw cycling more than three times, after which polymerization was performed at 70°C using a temperature-controlled heating mantle followed by stirring at 60 rpm for 2 h to reach nearly full conversion. A sample was extracted from the polymerization medium using a degassed syringe for ¹H NMR and GPC analyses to determine the monomer conversion, $M_{n,GPC}$, and \bar{D} values.

Synthesis of poly(2-acrylamido-2-methyl-1-propanesulfonic acid (AMPS)). Phosphate buffer solution (6 mL, 10 mM, pH = 7), CETCPA (17.9 mg, 6.08 mM), AMPS (1725 mg, 0.87 M), and V-50 (2.0 mg, 0.77 mM) were introduced into a 100-mL flask equipped with a magnetic stirrer bar and sealed with a rubber septum to synthesize poly(AMPS). The mixture was deoxygenated by freeze–pump–thaw cycling more than three times, after which polymerization was performed at 70°C using a temperature-controlled heating mantle followed by stirring at 60 rpm for 2 h to reach nearly full conversion. A sample was extracted from the polymerization medium using a degassed syringe for ¹H NMR and GPC analyses to determine the monomer conversion, $M_{n,GPC}$, and \bar{D} values.

Synthesis of subsequent blocks. For the subsequent block extension, the deoxygenated monomer, initiator, and solvent mixture were injected into the polymerization medium (the detailed conditions are listed in Supplementary Tables 1, 3, 5, 7, 9, and 11). The resultant mixture was polymerized at 70°C using a temperature-controlled heating mantle followed by stirring at 60 rpm for 2 h to reach nearly full conversion. Before each injection, a sample was extracted from the polymerization medium using a degassed syringe for ¹H NMR and GPC analyses to determine the monomer conversion, $M_{n,GPC}$, and \bar{D} values (see Supplementary Figs. 2–4 and Supplementary Tables 2, 4, 6, 8, 10 and 12).

Hydrogel preparation

Tri(LM)block, tri(SM)block, pentablock, and nonablock polyelectrolytes were prepared at 1.8 mM polymer concentration in 1.0 M NaCl solutions and mixed to match the 1:1 charge ratio. These solutions were dialyzed inside a 4-L plastic basket filled with 0.7, 0.3, 0 M NaCl solutions for 6 days (replaced every 2 days) using a dialysis membrane with pre-treated RC tubing (molecular weight cut-off: 10 kDa, diameter: 29 mm) to reach the salt-free hydrogels. The reason for making a

hydrogel by dialysis slowly in a salty sol state is to avoid the problem of phase fixation in an unequal network when two polymers having opposite charges are mixed at once. Thereafter, water was added to or removed from the abovementioned hydrogels to achieve target polymer concentrations. The hydrogel concentration was determined by comparing the weights of the swollen and dry samples.

NMR spectroscopy

^1H NMR spectra were recorded on a Bruker Avance III 500 spectrometer at 25° C and a frequency of 500 MHz. The delay time was set to 2.5 s. All polymer samples were prepared in D_2O . Chemical shift values (δ) were reported in ppm and determined with respect to non-deuterated solvent residues as internal references.

Determination of the monomer conversion. For the multiblock polyelectrolytes, monomer conversions were determined by comparing the decrease in the integrated intensity of the vinyl protons ($\delta = 6.70\text{--}5.70$ ppm) of the monomer with that of the *R* group protons ($\delta = 3.60\text{--}2.75$ ppm) of the monomer and polymer after polymerization by ^1H NMR.

Determination of the $M_{n,\text{th}}$ value. The theoretical number-average molar mass ($M_{n,\text{th}}$) was calculated as follows:

$$M_{n,\text{th}} = \frac{[M]_0 p M_M}{[CTA]_0} + M_{\text{CTA}}, \quad (1)$$

where $[M]_0$ and $[CTA]_0$ are the initial concentrations of the monomer and chain transfer agent, respectively, and p is the monomer conversion determined by ^1H NMR. M_M and M_{CTA} are the molar masses (g mol^{-1}) of the monomer and chain transfer agent, respectively.

GPC studies

Molar mass distributions were measured on a Shimadzu LC-20AD liquid chromatography system using dedicated columns for anionic and cationic polymers. For anionic polymers, an Agilent PL-aquagel-OH, 8 μm , MIXED-M column (300×7.5 mm) and Agilent PL-aquagel-OH, 8 μm , guard column (50×7.5 mm) were utilized. The mobile phase consisted of 90% 0.15 M NaNO_3 aqueous solution and 10% methanol. The flow rate was 1.0 mL min^{-1} , and the temperature was 40° C. The instrument was calibrated with low-dispersity poly(ethyleneoxide) standards (Scientific Polymer) whose molar masses varied between 0.2 and 800 kg mol^{-1} . For cationic polymers, TOSOH TSKgel, 10 μm , G5000PWXL-CP column (300×7.8 mm) and TOSOH TSKgel, 13 μm , PWXL-CP guard column (40×6 mm) were used. The mobile phase consisted of 0.3 M NaNO_3 aqueous solution with pH = 3 adjusted by sulfuric acid. The flow rate was 1.0 mL min^{-1} and the temperature was 40° C. The instrument was calibrated with low-dispersity poly(ethyleneoxide) standards (Scientific Polymer) whose molar masses varied between 0.2 and 800 kg mol^{-1} . Analyte samples were filtered through a polyvinylidene fluoride membrane with 0.2- μm pores before injection. The experimental molar mass ($M_{n,\text{GPC}}$) and dispersity (\bar{D}) values of the synthesized polymers were determined by conventional calibration using the LC Solution software with a known RI detector calibration constant.

Multiangle light scattering

Dynamic light scattering (DLS) measurements were conducted using a BI-200SM goniometer (Brookhaven Instruments) equipped with a laser of a wavelength (λ) of 639 nm. Prior to measurements, all 0.2 wt% PEC solutions were filtered through 0.45 μm PTFE filters and then loaded into borosilicate glass tubes 10 mm in diameter. The sample cells were subsequently placed into a reservoir containing dust-free decalin, and the temperature was maintained at 25° C using a circulation bath. For DLS measurements, the intensity autocorrelation

functions ($g^{(2)}(q, t)$) were recorded at angles of $\theta = 30, 60, 90$, and 120° . The cumulant expression as shown in Eq. (2) was used to fit the $g^{(2)}(q, t)$ to extract the mean decay rate ($\bar{\Gamma}$)⁴⁹

$$g^{(2)}(q, t) - 1 = A \exp(-2\bar{\Gamma}t) \left[1 + \frac{\mu_2}{2!} t^2 + \dots \right]^2, \quad (2)$$

The mutual diffusion coefficient (D_m) was determined by linear regression of $\bar{\Gamma} = D_m q^2$. The hydrodynamic radius (R_h) was calculated using the Stokes-Einstein equation, $R_h = k_B T / 6\pi\eta_0 D_m$, where k_B , T , and η_0 are the Boltzmann constant, absolute temperature, and solvent viscosity, respectively.

Cryo-TEM measurements

0.2 wt% of tri(LM)-, tri(SM)-, penta- and nona-PEC for cryo-TEM analysis were prepared at 21° C with humidity of 100 % using a Vitrobot Mark IV (Thermo Fisher Scientific, Waltham, MA, USA). Samples (3.5 μL) were applied onto a UV- O_3 -treated lacey carbon-supported copper grid and then blotted for 2–3 sec to remove an excess solution before rapid vitrification by plunge-freezing the grids into liquid ethane at its melting temperature ($\sim -183^\circ \text{C}$). Grids were transferred to a Gatan cryo stage and imaged using JEM-1400 (JEOL Ltd., Tokyo, Japan) operating at 120 kV equipped with a Gatan 914 cryo-holder (Gatan Inc., Pleasanton, CA, USA). TEM images were recorded and analyzed using a Xarosa bottom-mounted CMOS camera (EMSIS GmbH, Münster, Germany) and RADIUS software (Olympus-SiS, Münster, Germany).

SANS measurements

Small-angle neutron scattering (SANS) measurements were carried out by the SANS-U diffractometer at the Institute for Solid State Physics, the University of Tokyo, installed in the neutron guide hall at the JRR-3 research reactor of the Japan Atomic Energy Agency in Tokai, Japan^{50,51}. The measurements were conducted at 4 m sample-to-detector lengths by using neutrons of 7.0 Å wavelength with $\Delta\lambda/\lambda = 0.10$ full-width at half-maximum, which covered the scattering wavenumbers Q range from 0.007 to 0.1 Å^{-1} and the exposure time was 1800 s. The scattered neutrons were detected by a 2D multiwired ^3He detector. After data corrections, including dark counts subtraction and cell-scattering subtraction, the obtained data sets were then normalized to an absolute scale using the incoherent scattering of a polyethylene thin plate as a standard sample and circular averaging of the two-dimensional data and incoherent scattering subtraction proceeded. All measurements were performed at 25° C using 0.2 wt% PEC dissolved in D_2O .

Rheological measurements

Rheological experiments were performed on a DHR-2 rheometer (TA Instruments) using a parallel plate with a diameter of 20 mm. The rheometer was equipped with a Peltier heating system with an environmental enclosure for temperature control. The rheological strain amplitude sweep was performed from 1 to 1000% at a frequency of 3 rad s^{-1} , which was sufficiently low to exclude the shear rate-dependent effects. Frequency sweep was conducted at frequencies ranging from 0.1 to 100 rad s^{-1} and a strain of 1%, which corresponded to the linear viscoelastic regime according to the results of strain sweep experiments. Zero-shear viscosity was confirmed at a shear rate of 0.0005 s^{-1} . Cyclic strain jump tests were conducted at strains between 1% and 1000% and a frequency of 3 rad s^{-1} . All measurements were performed at 25° C using dialyzed PEC hydrogels.

SAXS measurements

SAXS experiments were performed using the 3 C beamline of the Pohang Accelerator Laboratory containing a MAR CCD detector with a q -range of $0.006\text{--}0.13 \text{ Å}^{-1}$, where the wave vector q was defined as $q = 4\pi\lambda^{-1}\sin(\theta/2)$. PEC hydrogel samples for SAXS measurements were

placed in the cell at the concentrations utilized in the rheological experiments. The sample-to-detector distance was 2.92 m, and the exposure time was set to 30 s. All measurements were performed at 25°C using dialyzed PEC hydrogels. The background was subtracted from the hydrogel scattering profiles. The obtained SAXS data were processed and analyzed with the EasyPlot software.

Data availability

The data that support the findings of this study are included in the published article (and its Supplementary Information) or available from the corresponding author on request.

References

- Yang, Y. J., Holmberg, A. L. & Olsen, B. D. Artificially engineered protein polymers. *Annu. Rev. Chem. Biomol. Eng.* **8**, 549–575 (2017).
- Mendes, A. C., Baran, E. T., Reis, R. L. & Azevedo, H. S. Self-assembly in nature: using the principles of nature to create complex nanobiomaterials. *Wiley Interdiscip. Rev. Nanomed. Nanobiotechnol.* **5**, 582 (2013).
- Gong, B., Wei, X., Qian, J. & Lin, Y. Modeling and simulations of the dynamic behaviors of actin-based cytoskeletal networks. *ACS Biomater. Sci. Eng.* **5**, 3720 (2019).
- Chen, J., Ahn, T., Colón-Bernal, I. D., Kim, J. & Banaszak Holl, M. M. The relationship of collagen structural and compositional heterogeneity to tissue mechanical properties: A chemical perspective. *ACS Nano* **11**, 10665 (2017).
- Demouveau, B., Gouyer, V., Gottrand, F., Narita, T. & Desseyn, J. L. Gel-forming mucin interactome drives mucus viscoelasticity. *Adv. Colloid Interface Sci.* **252**, 69 (2018).
- Rubinstein, M., Colby, R. *Polymer Physics.*, (Oxford, 2003).
- Sakai, T., ed. *Physics of polymer gels.*, (John Wiley & Sons, 2020).
- Du, X., Zhou, J. & Shi, J. Xu, B. Supramolecular hydrogelators and hydrogels: From soft matter to molecular biomaterials. *Chem. Rev.* **115**, 13165 (2015).
- Elkema, R. & Pich, A. Pros and cons: supramolecular or macro-molecular: What is best for functional hydrogels with advanced properties? *Adv. Mater.* **32**, e1906012 (2020).
- Sautaux, J., Marx, F., Gunkel, I., Weder, C. & Schrettl, S. Mechanically robust supramolecular polymer co-assemblies. *Nat. Commun.* **13**, 1 (2022).
- Zhang, Z. et al. Mechanically interlocked networks cross-linked by a molecular necklace. *Nat. Commun.* **13**, 1 (2022).
- Ke, H. et al. Shear-induced assembly of a transient yet highly stretchable hydrogel based on pseudopolyrotaxanes. *Nat. Chem.* **11**, 470 (2019).
- Gu, Y., Zhao, J. & Johnson, J. A. A (Macro)molecular-level understanding of polymer network topology. *Trends Chem.* **1**, 318 (2019).
- Gu, Y., Zhao, J. & Johnson, J. A. Polymer networks: from plastics and gels to porous frameworks. *Angew. Chem. Int. Ed.* **59**, 5022 (2020).
- Nishi, K., Fujii, K., Chung, U., Shibayama, M. & Sakai, T. Experimental observation of two features unexpected from the classical theories of rubber elasticity. *Phys. Rev. Lett.* **119**, 1 (2017).
- Lang, C. et al. Solvent-non-solvent rapid-injection for preparing nanostructured materials from micelles to hydrogels. *Nat. Commun.* **10**, 1 (2019).
- Srivastava, S., Levi, A. E., Goldfeld, D. J. & Tirrell, M. V. Structure, morphology, and rheology of polyelectrolyte complex hydrogels formed by self-assembly of oppositely charged triblock polyelectrolytes. *Macromolecules* **53**, 5763 (2020).
- Kim, J. M., Heo, T. Y. & Choi, S. H. Structure and relaxation dynamics for complex coacervate hydrogels formed by ABA triblock copolymers. *Macromolecules* **53**, 9234 (2020).
- Hunt, J. N. et al. Tunable, high modulus hydrogels driven by ionic coacervation. *Adv. Mater.* **23**, 2327 (2011).
- Sliozberg, Y. R. et al. Modeling viscoelastic properties of triblock copolymers: A DPD simulation study. *J. Polym. Sci. Part B Polym. Phys.* **48**, 15 (2010).
- Li, N. K. et al. Salt responsive morphologies of ssDNA-based triblock polyelectrolytes in semi-dilute regime: effect of volume fractions and polyelectrolyte length. *Macromol. Rapid Commun.* **38**, 1 (2017).
- Srivastava, S. et al. Gel phase formation in dilute triblock copolyelectrolyte complexes. *Nat. Commun.* **8**, 1 (2017).
- Zhou, C., Hillmyer, M. A. & Lodge, T. P. Efficient formation of multicompartment hydrogels by stepwise self-assembly of thermo-responsive ABC triblock terpolymers. *J. Am. Chem. Soc.* **134**, 10365 (2012).
- Shen, W., Zhang, K., Kornfield, J. A. & Tirrell, D. A. Tuning the erosion rate of artificial protein hydrogels through control of network topology. *Nat. Mater.* **5**, 153 (2006).
- Balsara, N. P., Tirrell, M. & Lodge, T. P. Micelle formation of BAB triblock copolymers in solvents that preferentially dissolve the A block. *Macromolecules* **24**, 1975 (1991).
- Monzen, M., Kawakatsu, T., Doi, M. & Hasegawa, R. Micelle formation in triblock copolymer solutions. *Comput. Theor. Polym. Sci.* **10**, 275 (2000).
- Bray, C., Peltier, R., Kim, H., Mastrangelo, A. & Perrier, S. Anionic multiblock core cross-linked star copolymers via RAFT polymerization. *Polym. Chem.* **8**, 5513 (2017).
- Gody, G., Maschmeyer, T., Zetterlund, P. B. & Perrier, S. Rapid and quantitative one-pot synthesis of sequence-controlled polymers by radical polymerization. *Nat. Commun.* **4**, 1 (2013).
- Gody, G., Maschmeyer, T., Zetterlund, P. B. & Perrier, S. Pushing the limit of the RAFT process: multiblock copolymers by one-pot rapid multiple chain extensions at full monomer conversion. *Macromolecules* **47**, 3451 (2014).
- Sfika, V. & Tsitsilianis, C. Association phenomena of poly(acrylic acid)-b-poly(2-vinylpyridine)-b-poly(acrylic acid) triblock polyampholyte in aqueous solutions: From transient network to compact micelles. *Macromolecules* **36**, 4983 (2003).
- Fukushima, T. et al. Molecular ordering of organic molten salts triggered by single-walled carbon nanotubes. *Science* **300**, 2072 (2003).
- Gula, I. A., Karimi-Varzaneh, H. A. & Svaneborg, C. Computational study of cross-link and entanglement contributions to the elastic properties of model PDMS networks. *Macromolecules* **53**, 6907 (2020).
- Svaneborg, C., Everaers, R., Grest, G. S. & Curro, J. G. Connectivity and entanglement stress contributions in strained polymer networks. *Macromolecules* **41**, 4920 (2008).
- Eom, Y., Park, Y., Jung, Y. M. & Kim, B. C. Effects of conformational change of polyacrylonitrile on the aging behavior of the solutions in N,N-dimethyl formamide. *Polymer* **108**, 193 (2017).
- Noda, I. Determination of two-dimensional correlation spectra using the Hilbert transform. *Appl. Spectrosc.* **54**, 994 (2000).
- Park, Y., Jin, S., Noda, I. & Jung, Y. M. Emerging developments in two-dimensional correlation spectroscopy (2D-COS). *J. Mol. Struct.* **1217**, 128405 (2020).
- Lasch, P. & Noda, I. Two-dimensional correlation spectroscopy (2D-COS) for analysis of spatially resolved vibrational spectra. *Appl. Spectrosc.* **73**, 359 (2019).
- Li, W. & Wu, P. Unusual thermal phase transition behavior of an ionic liquid and poly(ionic liquid) in water with significantly different LCST and dynamic mechanism. *Polym. Chem.* **5**, 5578 (2014).
- Chung, T. et al. Effect of anions on the phase transition temperature of two structurally isomeric polymers: poly(N-isopropylacrylamide) and poly(2-isopropyl-2-oxazoline). *Polym. Chem.* **13**, 4615 (2022).

40. Geitner, R. et al. Hydrogel-embedded model photocatalytic system investigated by Raman and IR spectroscopy assisted by density functional theory calculations and two-dimensional correlation analysis. *J. Phys. Chem. A* **122**, 2677 (2018).
41. Koo, J. M. et al. Nonstop monomer-to-aramid nanofiber synthesis with remarkable reinforcement ability. *Macromolecules* **52**, 923 (2019).
42. Sun, S. & Wu, P. From globules to crystals: a spectral study of poly(2-isopropyl-2-oxazoline) crystallization in hot water. *Phys. Chem. Chem. Phys.* **17**, 32232 (2015).
43. Li, T., Tang, H. & Wu, P. Molecular evolution of poly(2-isopropyl-2-oxazoline) aqueous solution during the liquid-liquid phase separation and phase transition process. *Langmuir* **31**, 6870 (2015).
44. Choi, J., Yoon, J., Ahn, K. H., Choi, S. H. & Char, K. Injectable hydrogels with improved mechanical property based on electrostatic associations. *Colloid Polym. Sci.* **299**, 575 (2021).
45. Derkach, S. R., Voron'ko, N. G. & Sokolan, N. I. The rheology of hydrogels based on chitosan-gelatin (bio)polyelectrolyte complexes. *Sci. Technol.* **38**, 1427 (2017).
46. Netter, A. B., Goudoulas, T. B. & Germann, N. Effects of bloom number on phase transition of gelatin determined by means of rheological characterization. *Lwt* **132**, 109813 (2020).
47. Zepa, A., Pakzad, L. & Fatehi, P. Hardwood kraft lignin-based hydrogels: production and performance. *ACS Omega* **3**, 8233 (2018).
48. O'Leary, L. E. R., Fallas, J. A., Bakota, E. L., Kang, M. K. & Hartgerink, J. D. Multi-hierarchical self-assembly of a collagen mimetic peptide from triple helix to nanofiber and hydrogel. *Nat. Chem.* **3**, 821 (2011).
49. Koppel, D. E. Analysis of macromolecular polydispersity in intensity correlation spectroscopy: the method of cumulants. *J. Chem. Phys.* **57**, 4814 (1972).
50. Okabe, S., Karino, T., Nagao, M., Watanabe, S. & Shibayama, M. Current status of the 32 m small-angle neutron scattering instrument, SANS-U. *Nucl. Instrum. Methods Phys. Res. Sect. A Accel. Spectrometers Detect. Assoc. Equip.* **572**, 853 (2007).
51. Endo, H., Mayumi, K., Osaka, N., Ito, K. & Shibayama, M. The static structure of polyrotaxane in solution investigated by contrast variation small-angle neutron scattering. *Polym. J.* **43**, 155 (2011).

Acknowledgements

This work was financially supported by the National Research Foundation of Korea (NRF) grant funded by the Korea government (MSIT) (No. RS-2024-00408989, RS-2024-00408795, 2022R1A2C2012889). The computational part was supported by the MRSEC Program of the National Science Foundation under Award No. DMR 2308708 (IRG-2). MD used resources of the Extreme Science and Engineering Discovery Environment (XSEDE, supported by the NSF Project TG- MCA05S027) and the computational facilities purchased with funds from the National Science Foundation (CNS-1725797) and administered by the Center for Scientific Computing (CSC). The CSC is supported by the California NanoSystems Institute and the Materials Research Science and Engineering Center (MRSEC; NSF DMR 2308708) at UC Santa Barbara. The SANS measurements were carried out at JRR-3 with the general user program managed by the Institute for Solid State Physics, The University of Tokyo (proposal number:23404). The authors wish to thank

Prof. Dong Soo Hwang for their helpful discussions and comments on the paper.

Author contributions

J.H. designed and performed the experiments. S.N. performed and analyzed CG-MD simulations. J.H. and J.M.K. performed and analyzed Raman experiments and 2DCOS analysis. J.H., T.C., I.K.H., and J.K. performed and discussed SAXS experiments. L.G. and K.M. performed and analyzed SANS experiments. J.H., S.H.O., and S.H.C. performed and analyzed multiangle DLS experiments. Y.B., J.P., and E.L. performed and discussed Cryo-TEM experiments. J.H., S.C., D.W.C., and J.J. performed and discussed rheological experiments. J.H., S.N., U.J., J.-E.S., G.H.F., and Y.S.K. analyzed and discussed all data. J.H., S.N., J.-E.S., and Y.S.K. wrote the manuscript. Y.S.K. supervised the overall progress of this manuscript preparation. All authors read and approved the final manuscript.

Competing interests

The authors declare no competing interests.

Additional information

Supplementary information The online version contains supplementary material available at <https://doi.org/10.1038/s41467-024-50902-z>.

Correspondence and requests for materials should be addressed to Eunji Lee, Joan-Emma Shea or Youn Soo Kim.

Peer review information *Nature Communications* thanks Andrij Pich and the other anonymous reviewers for their contribution to the peer review of this work. A peer review file is available.

Reprints and permissions information is available at <http://www.nature.com/reprints>

Publisher's note Springer Nature remains neutral with regard to jurisdictional claims in published maps and institutional affiliations.

Open Access This article is licensed under a Creative Commons Attribution-NonCommercial-NoDerivatives 4.0 International License, which permits any non-commercial use, sharing, distribution and reproduction in any medium or format, as long as you give appropriate credit to the original author(s) and the source, provide a link to the Creative Commons licence, and indicate if you modified the licensed material. You do not have permission under this licence to share adapted material derived from this article or parts of it. The images or other third party material in this article are included in the article's Creative Commons licence, unless indicated otherwise in a credit line to the material. If material is not included in the article's Creative Commons licence and your intended use is not permitted by statutory regulation or exceeds the permitted use, you will need to obtain permission directly from the copyright holder. To view a copy of this licence, visit <http://creativecommons.org/licenses/by-nc-nd/4.0/>.

© The Author(s) 2024